Analysis of measurement errors for a superconducting phase qubit

Qin Zhang,[1] Abraham G. Kofman,[1,] [*] John M. Martinis,[2] and Alexander N. Korotkov[1]

[1]*Department of Electrical Engineering, University of California, Riverside, California 92521*
[2]*Department of Physics, University of California, Santa Barbara, California 93106*
(Dated: February 6, 2008)

We analyze several mechanisms leading to errors in a course of measurement of a superconducting flux-biased phase qubit. Insufficiently long measurement pulse may lead to nonadiabatic transitions between qubit states $|1\rangle$ and $|0\rangle$, before tunneling through a reduced barrier is supposed to distinguish the qubit states. Finite (though large) ratio of tunneling rates for these states leads to incomplete discrimination between $|1\rangle$ and $|0\rangle$. Insufficiently fast energy relaxation after the tunneling of state $|1\rangle$ may cause the repopulation of the quantum well in which only the state $|0\rangle$ is supposed to remain. We analyze these types of measurement errors using analytical approaches as well as numerical solution of the time-dependent Schrödinger equation.

I. INTRODUCTION

In recent years, a significant progress has been made in developing superconducting Josephson-junction circuits for quantum computation. Single-qubit[1,2,3] and coupled-qubit[4,5,6] operations have been demonstrated for various qubit types, including charge,[1,4] flux,[2] and phase[2,5,6,7,8,9] qubits. Recently introduced flux-biased phase qubits[6,7,8,9] (Fig. 1) significantly reduce the total dissipation during measurement in comparison with the current-biased phase qubits,[3,5] which leads to lower decoherence and faster recovery after measurement.

Measurement of qubits is an important stage in quantum information processing. A novel scheme for fast measurements of flux-biased phase qubits has been demonstrated[7] and subsequently employed for simultaneous measurement of two coupled qubits.[6] According to this scheme [see Fig. 1(b)], a measurement is performed by lowering the barrier between the qubit "left" potential well and a much deeper "right" well, so that tunneling from qubit state $|1\rangle$ (the first excited left-well state) to the right well occurs with probability close to one, while state $|0\rangle$ (the left-well ground state) remains intact.

It is of interest to analyze the measurement process theoretically, since such an analysis can be used to minimize measurement errors. In measurements of coupled qubits, there are generally one- and two-qubit errors. The main source of two-qubit errors is crosstalk,[6] arising after the application of the measurement pulse due to the coupling between the qubits. The crosstalk was analyzed by us recently.[10]

The present paper is devoted to the theoretical study of the behavior of a single flux-biased phase qubit during the measurement pulse, which lowers the barrier. Our purpose is to find potential sources of one-qubit measurement errors in the fast measurement scheme used in Refs. 6 and 7, and analyze relations between the error level and the parameters of the measurement pulse. We consider three mechanisms of single-qubit errors. First, there is a possibility of transitions between qubit states $|1\rangle$ and $|0\rangle$ due to nonadiabaticity of the process. Second,
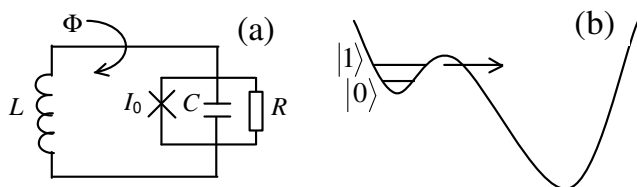

FIG. 1: (a) Circuit schematic of the flux-biased phase qubit, controlled by external magnetic flux $\phi(t)$. (b) Sketch of the qubit potential energy $U(\delta)$, where δ is the superconducting phase difference across the Josephson junction. During the measurement pulse the energy barrier is lowered so that the state $|1\rangle$ escapes from the "left" well into the neighboring "right" well; this escape is sensed by a nearby SQUID.

there may be an incomplete discrimination between the two qubit states by tunneling. Third, it happens that if the after-tunneling energy relaxation is not fast enough, there is a possibility of a repopulation of the left qubit well (in which only the state $|0\rangle$ is supposed to remain) after tunneling of the state $|1\rangle$ to the right well.

The paper is organized as follows. Section II contains a discussion of flux-biased phase qubits, measurement errors, and the method for numerical solution of the Schrödinger equation used in the paper. Nonadiabatic effects are studied in Sec. III, where we derive analytical formulas and perform numerical calculations. The efficiency of the qubit state discrimination by tunneling is discussed in Sec. IV. The repopulation error mechanism is discussed in Sec. V, where we perform full numerical simulation of the quantum evolution in absence of energy dissipation, and estimate the rate of dissipation required to eliminate the repopulation effect. Finally, Sec. VI contains concluding remarks.

II. MODEL

The flux-biased phase qubit [Fig. 1(a)] has the same circuit schematic as the rf SQUID.[11] In its quantum de-

scription the wavefunction $\Psi(\delta,t)$ evolves according to the Schrödinger equation with the Hamiltonian

$$H(t) = \frac{\hat{p}^2}{2m} + U(\delta,t), \qquad (1)$$

where δ is the superconducting phase difference across the Josephson junction, $\hat{p} = -i\hbar(\partial/\partial\delta)$ is the momentum operator, $m = [\Phi_0/(2\pi)]^2 C$ is the effective mass, C is the junction capacitance, $\Phi_0 = h/(2e)$ is the flux quantum, e is the electron charge, and the qubit potential is

$$U(\delta,t) = E_J \left\{ \frac{[\delta - \phi(t)]^2}{2\lambda} - \cos\delta \right\}, \qquad (2)$$

where $E_J = I_0 \Phi_0/(2\pi)$ is the Josephson energy, $\lambda = 2\pi I_0 L/\Phi_0$ is the dimensionless inductance, $\phi(t) = 2\pi\Phi(t)/\Phi_0$ is the dimensionless external magnetic flux, $\Phi(t)$ is the magnetic flux in the loop, I_0 is the critical current, and L is the inductance. We will assume that before the measurement pulse the right well of the qubit potential [see Fig. 1(b)] is much deeper than the left well (as in Refs. 6,7,8,9). The qubit levels $|0\rangle$ and $|1\rangle$ are, respectively, the ground and the first excited levels in the left well.

The depth $\Delta U_{l,r}$ of a left (l) or right (r) well (i.e. the energy difference between the potential maximum and minimum) depends on external flux ϕ and can be characterized by the estimated number of the discrete levels in the well:

$$N_{l,r} = \frac{\Delta U_{l,r}}{\hbar\omega_{l,r}}, \qquad (3)$$

where $\omega_{l,r}$ is the classical oscillation frequency near the well bottom (the "plasma frequency"), $\omega_{l,r} = \sqrt{E_J(1/\lambda + \cos\delta_{l,r})/m}$ (here $\delta_{l,r}$ corresponds to the well bottom). The energy dissipation in the phase qubit can be described by introducing resistance R into the circuit [Fig. 1(a)]; however, for the most of this paper the dissipation is neglected ($R = \infty$).

The fast qubit state measurement[7] is achieved by applying a pulse of the magnetic flux ϕ, which lowers sufficiently slowly (adiabatically) the barrier height ΔU_l (and so N_l), until the first excited state $|1\rangle$ of the qubit left well becomes very close to the barrier top, so that the system in this state can easily tunnel through the barrier to the right well, while tunneling from the ground state $|0\rangle$ is almost negligible. (In principle, the measurement can be arranged in a way so that the state $|1\rangle$ goes over the barrier; however, in this case tunneling from the state $|0\rangle$ becomes significant.) After the measurement pulse the potential $U(\delta)$ is returned to its initial shape by decreasing ϕ back to its value before the measurement. Ideally, the system initially in the upper qubit state $|1\rangle$ should switch after the measurement to the right well, while the qubit initially in the ground state $|0\rangle$ should remain in the left well. However, at least two kinds of errors are possible in this process of qubit measurement. First, finite duration of the measurement pulse (which is

supposed to be rather fast) and corresponding nonadiabatic effects during increase of the flux $\phi(t)$, may lead to transitions between levels $|1\rangle$ and $|0\rangle$ (and other levels) before the tunneling starts. Second, during the tunneling stage the qubit in the state $|1\rangle$ may erroneously remain in the left well and/or state $|0\rangle$ may erroneously switch to the right well. One reason for the second type of error is finite ratio of tunneling rates for the states $|1\rangle$ and $|0\rangle$ (ideally, it should be infinitely large). Another reason is the incomplete switching of the state $|1\rangle$ due to repopulation of the left well from the right well during or *after* the tunneling stage. These kinds of errors will be considered in the following sections.

To solve numerically the time-dependent Schrödinger equation, we use the multi-projection approach of Ref. 12. In more detail, we divide the pulse duration τ into small time increments Δt and at each moment $t_k = k\Delta t$ ($k = 0, 1, \dots$) we find the eigenvalues E_n^k and eigenfunctions $\psi_n^k(\delta)$ for the Hamiltonian $H(t_k)$, using the Fourier grid Hamiltonian method[13] (equivalently, the periodic pseudospectral[14] method). Then the wavefunction is computed as

$$\Psi(\delta,t) = \sum_n a_n^k \psi_n^k(\delta)\, e^{-iE_n^k(t-t_k)/\hbar} \quad (t_k \leq t \leq t_{k+1}),$$

$$\qquad (4)$$

where

$$a_n^k = \int_{-\infty}^{\infty} [\psi_n^k(\delta)]^* \, \Psi(\delta,t_k)\, d\delta \qquad (5)$$

is calculated using the wavefunction $\Psi(\delta,t_k)$ at the end of the previous timestep. Starting the evolution from the initial qubit level i, we calculate the evolving population of the level n as

$$P_{ni}(t) = |a_n^k|^2, \quad \text{for } t_k \leq t \leq t_{k+1}. \qquad (6)$$

III. NONADIABATIC EFFECTS

During the stage of rising flux ϕ (before the tunneling), the population of the state $|0\rangle$ is supposed to remain unchanged. (Notice that excitation of state $|1\rangle$ to higher levels does not lead to the measurement error.) However, since increase of ϕ is not infinitely slow, there may be nonadiabatic transitions between levels $|0\rangle$ and $|1\rangle$ (and/or higher levels) leading to measurement errors. Such nonadiabatic errors are discussed in this section.

For numerical calculations we use the circuit parameters of Ref. 6:

$$C = 700 \text{ fF}, \ L = 0.72 \text{ nH}, \ I_0 = 1.7 \text{ mkA}. \qquad (7)$$

Also, we assume that during the first half of the measurement pulse the left-well dimensionless barrier N (here and below we omit the subscript l) decreases from $N = 5$ to $N = 1.355$, which corresponds to ϕ varying from 5.09 to 5.31 (for $N = 1.355$ the state $|1\rangle$ is very close to the barrier top[15]).
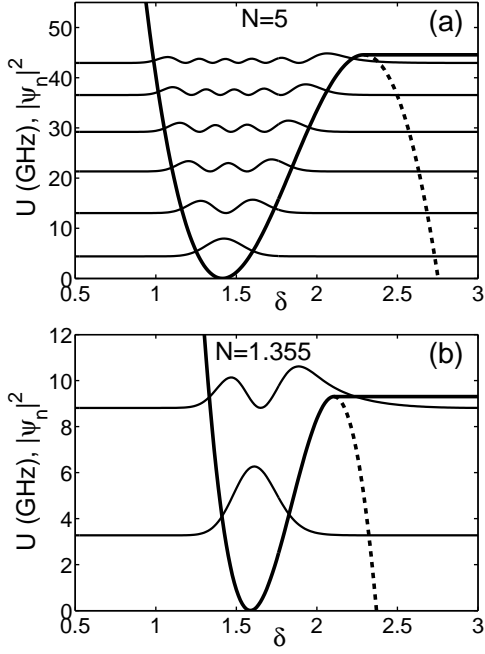
FIG. 2: The modified qubit potential (8) (thick solid lines, in GHz) and the normalized wavefunctions $|\psi_n(\delta)|^2$ (thin solid lines), shifted vertically by the energy eigenvalues E_n for (a) $N = 5$ and (b) $N = 1.355$; other qubit parameters are given by (7). Dashed lines correspond to the actual potential (2). The energy origin is chosen at the well minimum.

For simplicity, in this section we neglect tunneling. Correspondingly, we consider a modified potential energy (see Fig. 2), which differs from Eq. (2) by absence of the right well, so that the potential is constant to the right of the barrier-top position δ_b:

$$U(\delta, t) = \begin{cases} E_J\{(\delta - \phi)^2/2\lambda - \cos\delta\}, & \delta \leq \delta_b, \\ U(\delta_b, t), & \delta > \delta_b, \end{cases} \quad (8)$$

where both ϕ and δ_b change with time. In numerical calculations we limit the range of δ between 0.5 and 3, so that the wavefunction $\Psi(\delta, t)$ is assumed to vanish at $\delta = 0.5$ and $\delta = 3$ (we have checked that further increase of this range does not change the results). Figure 2 shows the wavefunctions $|\psi_n(\delta)|^2$ and energies E_n for the states localized in the well, corresponding to the beginning and the maximum of the measurement pulse. Since the nonadiabatic transitions after the tunneling stage are not important, in this section we consider only the first part of the measurement pulse (increase of ϕ, decrease of N).

A. Analytical theory

1. Nonadiabatic error

Assuming that the qubit wavefunction before the measurement is

$$|\Psi_0\rangle = c_0|\psi_0\rangle + c_1|\psi_1\rangle, \quad (9)$$

we describe the qubit evolution during the rising part of the measurement pulse by expanding its wavefunction over the instantaneous basis given by the eigenfunctions $\psi_n(\delta, t)$ of $H(t)$ with the eigenvalues $E_n(t)$:

$$\Psi(\delta, t) = \sum_n c_n(t) e^{-(i/\hbar)\int_0^t E_n(t')dt'} \psi_n(\delta, t); \quad (10)$$

the initial conditions are $c_0(0) = c_0$, $c_1(0) = c_1$, and $c_n(0) = 0$ for $n \geq 2$.

Let us define the nonadiabatic measurement error Q as the difference between the ground state occupation $P_0(t) = |\langle\psi_0(t)|\Psi(t)\rangle|^2$ before the measurement pulse $(t = 0)$ and at the maximum of the pulse $(t = \tau)$:

$$Q = |P_0(0) - P_0(\tau)|. \quad (11)$$

Here $P_0(0) = |c_0|^2$, while $P_0(\tau)$ can be expressed via the evolution operator $S(t)$ [so that $|\Psi(t)\rangle = S(t)|\Psi_0\rangle$]:

$$P_0(\tau) = |c_0|^2 P_{00}(\tau) + |c_1|^2 P_{01}(\tau)$$
$$+ 2\operatorname{Re}[c_0 c_1^* S_{00}(\tau) S_{01}^*(\tau)], \quad (12)$$

where $S_{ni}(\tau) = \langle\psi_n(\tau)|S(\tau)|\psi_i(0)\rangle$, while $P_{ni}(\tau) = |S_{ni}(\tau)|^2$ is the occupation of state n for initial state i. The last term in the rhs of Eq. (12) results from quantum interference.

We are interested in the case of a small nonadiabatic error, $Q \ll 1$. Then, as will be shown below, $S_{01}(\tau)$ and $1 - S_{00}(\tau)$ are quantities of the first and second order in the perturbation, respectively. Hence, up to the second order, the nonadiabatic error is given by

$$Q = |\,|c_0|^2[1 - P_{00}(\tau)] - |c_1|^2 P_{01}(\tau) - 2\operatorname{Re}[c_0 c_1^* S_{01}^*(\tau)]|, \quad (13)$$

Notice that $1 - P_{00}$ and P_{01} are both of the second order in perturbation; therefore in the case when both qubit states are initially occupied, the first two terms in Eq. (13) can be neglected in comparison with the third (interference) term. The third term is maximized when both qubit states are equally occupied, $|c_0| = |c_1| = 1/\sqrt{2}$, and $c_0 c_1^* S_{01}(\tau)$ is a real number. So, the maximum nonadiabatic error is approximately

$$Q_e = |S_{01}(\tau)| = \sqrt{P_{01}(\tau)}. \quad (14)$$

Notice that if initial state is $|\psi_1\rangle$, then the nonadiabatic error is $Q = P_{01}(\tau)$. If initial state is $|\psi_0\rangle$, then the error is $1 - P_{00}(\tau) = \sum_{n\geq 1} P_{n0}(\tau)$, which as will be seen later is approximately equal to $P_{01}(\tau)$ (because $P_{10} \approx P_{01}$ in

the lowest order, while P_{n0} for $n \geq 2$ are very small because direct transitions between non-neighboring levels are suppressed). Therefore, if only one qubit state is initially occupied, the error (in the lowest order) is

$$P_e = P_{01}(\tau) = Q_e^2, \qquad (15)$$

which is much smaller than Q_e. This fact can be easily understood by visualizing operator S as a rotation of the qubit Bloch sphere (neglecting higher levels). Then rotation by a small angle φ (around x-axis) leads to the change of z-coordinate by φ near equator (for $x = z = 0$), while the change is only $\varphi^2/2$ near the poles.

In this section we will mainly analyze the error P_e; however, it should be remembered that the actual nonadiabatic error can be up to $Q_e = \sqrt{P_e}$.

2. Adiabatic perturbation theory.

The evolution operator $S(t)$ obeys the Schrödinger equation, which can be reduced to the following form:[16,17]

$$\dot{S}_{ni} = \sum_{m \neq n} \frac{\langle \psi_n(t)|\dot{H}(t)|\psi_m(t)\rangle}{\hbar \omega_{nm}(t)} e^{i \int_0^t \omega_{nm}(t')dt'} S_{mi}, \quad (16)$$

where $\omega_{nm} = (E_n - E_m)/\hbar$. (The state label i appears only in indices, while i in the exponent is the imaginary unit.) The initial condition for Eq. (16) is $S_{ni}(0) = \delta_{ni}^K$, where δ_{ni}^K is the Kronecker symbol.

Equation (16) is exact. It can be simplified assuming slow variation of $H(t)$, so that $\dot{H}$ can be treated as a small perturbation. In the zero approximation (the adiabatic approximation[16,17]) the rhs of Eq. (16) is assumed to vanish, so that $\dot{S} = 0$ and therefore $S_{ni}(t) = \delta_{ni}^K$. In the first approximation we use $S_{mi} = \delta_{mi}^K$ in the rhs of Eq. (16), which yields[17] (for $n \neq i$)

$$S_{ni}(t) = \int_0^t dt' \frac{\langle \psi_n(t')|\dot{H}(t')|\psi_i(t')\rangle}{\hbar \omega_{ni}(t')} e^{i \int_0^{t'} \omega_{ni}(t'')dt''}. \qquad (17)$$

Notice that for $n \neq i$, $S_{ni}(t)$ is of the first order in perturbation, while $1 - S_{ii}(t)$ vanishes in the first order [see Eq. (16)], so that non-zero $1 - S_{ii}(t)$ appears only in the second order, when the first order S_{mi} is used in Eq. (16). Also notice that in the first order $S_{ni}(t) = -S_{in}^*(t)$, as follows from Eq. (17); therefore $P_{ni}(t) = P_{in}(t)$. We have used these properties in the previous subsection.

For the modified potential (8) we find

$$\dot{H}(t) = \dot{U}(\delta, t) = \begin{cases} E_J[\phi(t) - \delta]\dot{\phi}(t)/\lambda, & \delta \leq \delta_b(t); \\ dU(\delta_b(t), t)/dt, & \delta > \delta_b(t). \end{cases} \qquad (18)$$

For simplicity let us use the formula in the first line of Eq. (18) even at $\delta > \delta_b$ (this approximation can be justified by the fact that the wavefunctions are small to the right

of the barrier top position δ_b). Then the matrix elements of $\dot{H}$ can be calculated as

$$\langle \psi_n(t)|\dot{H}(t)|\psi_i(t)\rangle = -E_J \, \dot{\phi}(t) \, \delta_{ni}(t)/\lambda, \qquad (19)$$

where

$$\delta_{ni}(t) = \int_{-\infty}^{\infty} \psi_n^*(\delta, t) \, \delta \, \psi_i(\delta, t) \, d\delta \qquad (20)$$

is the "position" matrix element. Inserting Eq. (19) into (17), we obtain the following equation for $P_{ni}(t) = |S_{ni}(t)|^2$ ($n \neq i$) in the lowest order of perturbation:

$$P_{ni}(t) = \left(\frac{E_J}{\hbar\lambda}\right)^2 \left| \int_0^t dt' \frac{\dot{\phi}(t') \delta_{ni}(t')}{\omega_{ni}(t')} e^{i \int_0^{t'} \omega_{ni}(t'')dt''} \right|^2. \qquad (21)$$

Notice that for purely harmonic potential the matrix elements δ_{ni} are non-zero only for levels which are nearest neighbors. This means that P_{ni} for non-nearest neighbors would appear only in higher orders in perturbation. Since the qubit potential is not purely harmonic, there will be direct transitions between non-neighbors; however, these transition are significantly weaker than for nearest neighbors.

When the measurement pulse duration is scaled without change of the pulse shape, one can write the external flux as

$$\phi(t) \rightarrow \phi(t/\tau) = \phi(\theta), \qquad (22)$$

where τ is the duration of the rising part of the pulse and $\theta = t/\tau$. Then the Hamiltonian and hence its eigenstates and eigenvalues depend only on θ:

$$H(t) \rightarrow H(\theta), \quad \omega_{ni}(t) \rightarrow \omega_{ni}(\theta), \quad \psi_n(t) \rightarrow \psi_n(\theta). \quad (23)$$

As a result, Eq. (21) can be recast in the form

$$P_{ni}(t) = \left(\frac{E_J}{\hbar\lambda}\right)^2 \left| \int_0^\theta d\theta' \frac{\phi'(\theta')\delta_{ni}(\theta')}{\omega_{ni}(\theta')} e^{i\tau \int_0^{\theta'} \omega_{ni}(\theta'')d\theta''} \right|^2, \qquad (24)$$

where $\phi'(\theta) = d\phi(\theta)/d\theta$.

Finally, the nonadiabatic measurement error defined as $P_e = P_{01}(\tau)$ [see Eq. (15)] is obtained as

$$P_e = \left(\frac{E_J}{\hbar\lambda}\right)^2 \left| \int_0^1 d\theta \frac{\phi'(\theta)\delta_{10}(\theta)}{\omega_{10}(\theta)} e^{i\tau \int_0^\theta \omega_{10}(\theta')d\theta'} \right|^2. \qquad (25)$$

Even though this is only the lowest order approximation for $P_{01}(\tau)$, the numerical calculations of P_{01} show (see below) that Eq. (25) is quite accurate.

This formula for P_e can be further simplified (though with a noticeable loss of accuracy) by considering the qubit as a harmonic oscillator with the frequency ω_{10} changing in time. In this approximation[18]

$$\delta_{10} = \sqrt{\hbar/(2m\omega_{10})}, \qquad (26)$$

so Eq. (25) becomes

$$P_e = \frac{E_J^2}{2\hbar\lambda^2 m} \left| \int_0^1 d\theta \frac{\phi'(\theta)}{\omega_{10}^{3/2}(\theta)} e^{i\tau \int_0^\theta \omega_{10}(\theta')d\theta'} \right|^2. \quad (27)$$

This expression requires only the knowledge of the instantaneous transition frequency $\omega_{10}(t/\tau)$ and does not depend on the instantaneous wavefunctions.

Even further simplification is possible if we neglect the change of the frequency ω_{10} with time (as we see later, this is a quite crude approximation). Then the measurement error P_e is simply determined by the spectral component of the derivative ϕ' of the external flux at the frequency ω_{10}:

$$P_e = \frac{E_J^2}{2\hbar\lambda^2 m \omega_{10}^3} \left| \int_0^1 \phi'(\theta) e^{i\omega_{10}\tau\theta} d\theta \right|^2. \quad (28)$$

Since ω_{10} changes during the measurement pulse quite significantly (by more than 50 %, see Fig. 2), application of Eq. (28) is not straightforward and requires a choice of the time moment within the pulse, at which ω_{10} is taken. However, Eq. (28) can still be used for simple estimates of the nonadiabatic error, for example using the maximum and minimum values of ω_{10} (at the beginning of the pulse and at the end of its rising part). Notice that Eq. (28) implies that the nonadiabatic error can be significantly reduced by suppressing the spectral components of $\dot\phi(t)$ in the frequency range of ω_{10}.

3. Long-τ behavior.

In this subsection we analyze the asymptotic behaviour of the nonadiabatic measurement error P_e for long pulse duration τ, assuming that the pulse profile $\phi(t)$ is analytic everywhere except for the endpoints $t = 0$ and $t = \tau$. We show that in this case the long-τ behavior of P_e can be expressed via pulse properties at the singular (nonanalytic) endpoints.[19] Even though the result obtained below in this subsection cannot be directly applied to a realistic experiment, it still sheds a light on the dependence of the measurement error on the pulse shape.

The j-fold integration by parts of Eq. (17) yields

$$S_{ni}(\tau) = -\frac{e^{i\int_0^t \omega_{ni}(t')dt'}}{\omega_{ni}(t)} \sum_{k=1}^j i^k \frac{d^{k-1}}{dt^{k-1}}\left[\frac{g(t)}{\omega_{ni}^{k-1}(t)}\right]\Bigg|_0^\tau$$
$$+ i^j \int_0^\tau e^{i\int_0^t \omega_{ni}(t')dt'} \frac{d^j}{dt^j}\left[\frac{g(t)}{\omega_{ni}^j(t)}\right] dt, \quad (29)$$

where $g(t) = \langle\psi_n(t)|\dot H(t)|\psi_i(t)\rangle/\hbar\omega_{ni}(t)$ and the level label i again appears only in indices (i in other places is the imaginary unit). For scaling the pulse duration τ without change of a pulse shape, we use relation $d/dt = \tau^{-1}d/d\theta$ [see Eqs. (22) and (23)]; then the kth term in Eq. (29)

acquires a factor τ^{-k}. Let us denote by j_0 and j_1 the lowest orders of the time derivatives of the Hamiltonian, which do not vanish at $t = 0$ and τ, respectively. Then for sufficiently large τ, $(\min\omega_{ni})\tau \gg 1$, one can leave in Eq. (29) only the lowest-order nonvanishing terms corresponding to $t = 0$ and τ (θ=0 and 1) and obtain the approximation

$$S_{ni}(\tau) \approx \frac{i^{j_0}\langle\psi_n(0)|H^{(j_0)}(0)|\psi_i(0)\rangle}{\hbar\omega_{ni}^{j_0+1}(0)\tau^{j_0}}$$
$$- \frac{i^{j_1}\langle\psi_n(1)|H^{(j_1)}(1)|\psi_i(1)\rangle}{\hbar\omega_{ni}^{j_1+1}(1)\tau^{j_1}} e^{i\bar\omega_{ni}\tau}, \quad (30)$$

where time is normalized by τ, $H^{(j)}(\theta)$ is the jth derivative of $H(\theta)$, and $\bar\omega_{ni} = \int_0^1 \omega_{ni}(\theta)d\theta$ is the frequency averaged over the pulse duration.

Using the relation $\langle\psi_n(\theta)|H^{(j)}(\theta)|\psi_i(\theta)\rangle = -E_J\phi^{(j)}(\theta)\delta_{ni}(\theta)/\lambda$, which is similar to Eq. (19), we obtain the following approximation for the nonadiabatic error $P_e = |S_{01}(\tau)|^2$:

$$P_e \approx \frac{E_J^2}{\hbar^2\lambda^2\tau^{2j}} \left| \frac{\phi^{(j_0)}(0)\delta_{10}(0)}{\omega_{10}^{j_0+1}(0)\tau^{j_0-j}} \right.$$
$$\left. - \frac{i^{j_1-j_0}\phi^{(j_1)}(1)\delta_{10}(1)}{\omega_{10}^{j_1+1}(1)\tau^{j_1-j}} e^{i\bar\omega_{10}\tau} \right|^2, \quad (31)$$

where $j = \min\{j_0, j_1\}$. The error probability (31) generally decays with τ as τ^{-2j}. In particular, in the case $j_0 = j_1 = j$, Eq. (31) becomes

$$P_e \approx \frac{E_J^2}{\hbar^2\lambda^2\tau^{2j}} \left| \frac{\phi^{(j)}(0)\delta_{10}(0)}{\omega_{10}^{j+1}(0)} - \frac{\phi^{(j)}(1)\delta_{10}(1)}{\omega_{10}^{j+1}(1)} e^{i\bar\omega_{10}\tau} \right|^2. \quad (32)$$

In this case besides decaying with τ, the dependence $P_e(\tau)$ also oscillates with the frequency $\bar\omega_{10}$. In contrast, when $j_0 \neq j_1$, one of the two terms in Eq. (31) dominates at large τ, and the decay occurs monotonously.

4. Time-dependent perturbation theory

The approach used in subsection III A 2 can be compared with the standard time-dependent perturbation theory. Let us split the Hamiltonian (1) into the "unperturbed" Hamiltonian H_0 and "perturbation" $V(t)$:

$$H(t) = H_0 + V(t), \quad H_0 = \frac{\hat p^2}{2m} + U_0(\delta), \quad (33)$$

$$U_0(\delta) = E_J\left[\frac{(\delta - \phi_r)^2}{2\lambda} - \cos\delta\right], \quad (34)$$

$$V(t) = -(E_J/\lambda)[\phi(t) - \phi_r], \quad (35)$$

where we neglect the change of the energy origin and choose an arbitrary flux ϕ_r as a reference point. Even though the standard time-dependent perturbation

theory[18] can be only applied when the perturbation $V(t)$ is small, which is obviously not the case in our problem, let us still apply it formally. Then for the nonadiabatic error we obtain

$$P_e = \left(\frac{E_J \delta_{10}}{\hbar \lambda \omega_{10}}\right)^2 \left|\int_0^\tau \dot{\phi}(t) e^{i\omega_{10}t} dt\right|^2$$

$$= \left(\frac{E_J \delta_{10}}{\hbar \lambda \omega_{10}}\right)^2 \left|\int_0^1 \phi'(\theta) e^{i\omega_{10}\tau\theta} d\theta\right|^2, \qquad (36)$$

where δ_{10} and ω_{10} correspond to the Hamiltonian H_0. It is easy to see that Eq. (36) coincides with Eq. (25) if the time-dependence of δ_{10} and ω_{10} in Eq. (25) is neglected. An arbitrary choice of ϕ_r in the unperturbed Hamiltonian with a natural limitation $\phi(0) \le \phi_r \le \phi(\tau)$ corresponds to an arbitrary choice of the time moment within the pulse, at which δ_{10} and ω_{10} are taken.

Equation (36) can be simplified by using the approximation (26). Then it becomes exactly Eq. (28), which expresses P_e via the spectral component of the derivative of the external flux at the transition frequency ω_{10}. Even though this simplest result can be obtained in both approaches, we would like to emphasize that the approach of subsection III A 2 allows us to use much more accurate approximations for the error probability P_e.

B. Numerical results

For numerical calculations we use the method described in Section II [see Eqs. (4)–(6)]; which corresponds to the solution of exact equation (16). Let us describe the time dependence of the flux during the rising part of the measurement pulse as

$$\phi(t/\tau) = \phi_0 + (\phi_1 - \phi_0) \times g(t/\tau), \qquad (37)$$

where ϕ_0 and ϕ_1 are the initial and final flux values, while $g(\theta)$ describes the pulse shape and satisfies conditions $g(0) = 0$ and $g(1) = 1$. Unless mention otherwise, we choose in this subsection $\phi_0 = 5.09$ (corresponding to $N = 5$) and $\phi_1 = 5.31$ (corresponding to $N = 1.355$).

Consider first the simplest case of a linearly increasing pulse, $g(\theta) = \theta$. Figure 3 shows the time evolution of three quantities: P_{01}, P_{10}, and $1 - P_{00}$ (which all could in principle be used for the definition of the nonadiabatic error) for two values of the pulse duration: $\tau = 0.2$ ns and $\tau = 2$ ns. One can see that as expected, these three quantities practically coincide:

$$P_{01}(t) \approx P_{10}(t) \approx 1 - P_{00}(t), \qquad (38)$$

so that it is not really important which of them is used for the definition of the error P_e. (In this subsection for calculation of P_e we will use $1 - P_{00}$, which is slightly larger than two other quantities.) The dominating process is transitions between states $|0\rangle$ and $|1\rangle$; as a result, the oscillations in Fig. 3 are at the frequency $\omega_{10}(t)$ [see Eq. (21)]. The oscillation amplitude increases with time in
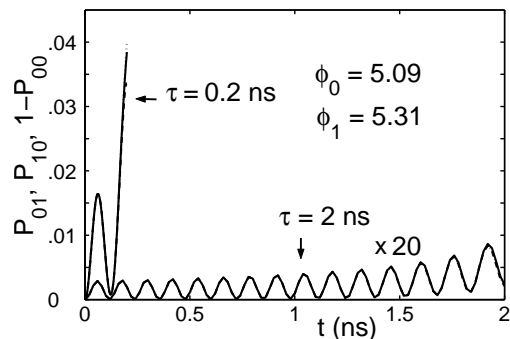

FIG. 3: Time dependence of the instantaneous nonadiabatic error defined in three different ways: $P_{01}(t)$ (solid lines), $P_{10}(t)$ (dashed lines), and $1 - P_{00}(t)$ (dotted lines), for two durations of the linear pulse: $\tau = 0.2$ ns and $\tau = 2$ ns (for $\tau = 2$ ns the data are multiplied by the factor 20). The solid, dashed, and dotted lines are practically indistinguishable, except near the pulse end for $\tau = 0.2$ ns.

Fig. 3. This is explained by the fact that increasing flux during the measurement pulse decreases the transition frequency ω_{10} (see Fig. 2), which leads to the increase of the integrand in Eq. (21) for $P_{01}(t)$ [note also Eq. (26)]; therefore, the oscillation amplitude should increase approximately as $[\omega_{10}(t)]^{-3}$. Figure 3 also demonstrates that the instantaneous nonadiabatic error is much larger for $\tau = 0.2$ ns than for $\tau = 2$ ns.

Figure 4 shows the dependence of the error P_e on the duration τ of the linear pulse on the double-logarithmic scale. The nonadiabatic error generally decreases with increase of τ (for linear pulse crudely as τ^{-2}); however, the dependence also shows oscillations, which originate from oscillations in Fig. 3. In Fig. 4(a) the thick solid line shows the numerical result. It is practically indistinguishable from the thin solid line showing the lowest-order analytical result (25). The dashed line corresponds to the simplified formula (27); one can see that it is also quite close to the exact result. We have observed a similar relation between the results obtained numerically, by analytical formula (25), and by simplified formula (27) for other pulse shapes discussed below. Figure 4(b) shows the dependence of the error on the pulse duration for three values of the final barrier height: $N = 1.355$, 1.5 and 1.65 (the initial value is $N = 5$ for all the cases). One can see that the error increases with the decrease of the final barrier height; however, dependence is not strong and therefore the results presented here are not quite sensitive to the exact choice of the pulse amplitude.

Figure 5 shows the comparison between the numerical results for $P_e(\tau)$ dependence and the results obtained using Eq. (28) which relates P_e to the spectral component of $\dot{\phi}$ at the frequency ω_{10}. Three panels of Fig. 5 are for (a) the linear pulse, (b) the pulse with shape $g(\theta) = 1 - \cos^4(\pi\theta/2)$, and (c) Gaussian pulse. (For Gaussian pulse we define τ as the r.m.s. width of the pulse; the fact that the pulse is really longer than τ, reduces P_e in comparison with other shapes.) The fre-
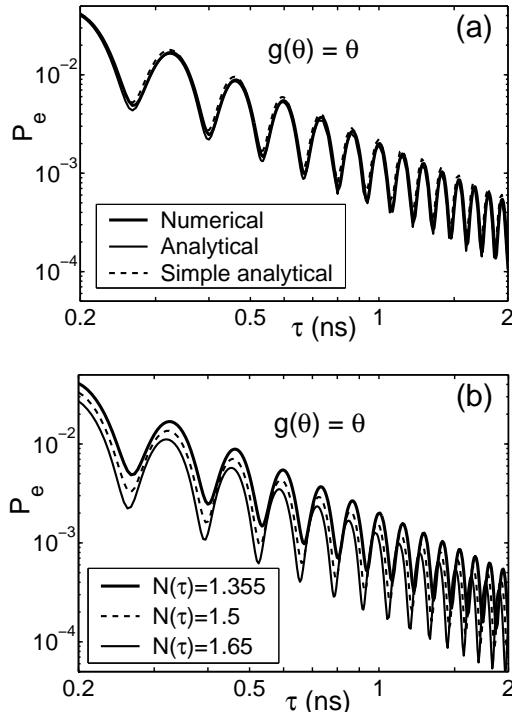
FIG. 4: The nonadiabatic error P_e as a function of the duration τ of the linear measurement pulse. (a) Numerical results (thick solid line) and results obtained using Eq. (25) (thin solid line) and Eq. (27) (dashed line) for the pulse starting with the barrier height $N = 5$ (corresponding to $\phi_0 = 5.09$) and ending with $N = 1.355$ ($\phi_1 = 5.308$). (b) Numerical results for pulses starting with $N = 5$ and ending with $N = 1.355$ (thick solid line), 1.5 (dashed line), and 1.65 (thin solid line); corresponding maximum fluxes are $\phi = 5.308$, 5.298, and 5.287.

quency ω_{10} in Eq. (28) is not well-defined since it changes during the pulse by more than 50%; so in Fig. 5 we show two analytical results, corresponding to ω_{10} at the beginning and at the end of the rising part of the pulse. One can see that in Fig. 5(a) the analytical curves show oscillations as well as the numerical curve; however, the amplitude of oscillations is much larger for the analytics (P_e goes to zero at some values of τ, in contrast to the numerical results). Neglecting oscillations, we see that the numerical curve is approximately in the middle between the two analytical curves (on the logarithmic scale). In contrast to that, in Fig. 5(b) the numerical curve is close to the lower analytical curve (and shows some oscillations, which are not well pronounced in the analytical results), while in Fig. 5(c) the numerical curve is close to the upper analytical line. As follows from the results in Fig. 5, even though Eq. (28) can be used for a simple estimate of the nonadiabatic error, the accuracy of this estimate can easily be worse than one order of magnitude. [The ratio between the upper and lower analytical estimates in Figs. 5(b) and 5(c) is crudely r_ω^7, where r_ω is the ratio of frequencies ω_{10} before and in the middle of the pulse; and even though $r_\omega \simeq 1.6$ is not a big number,
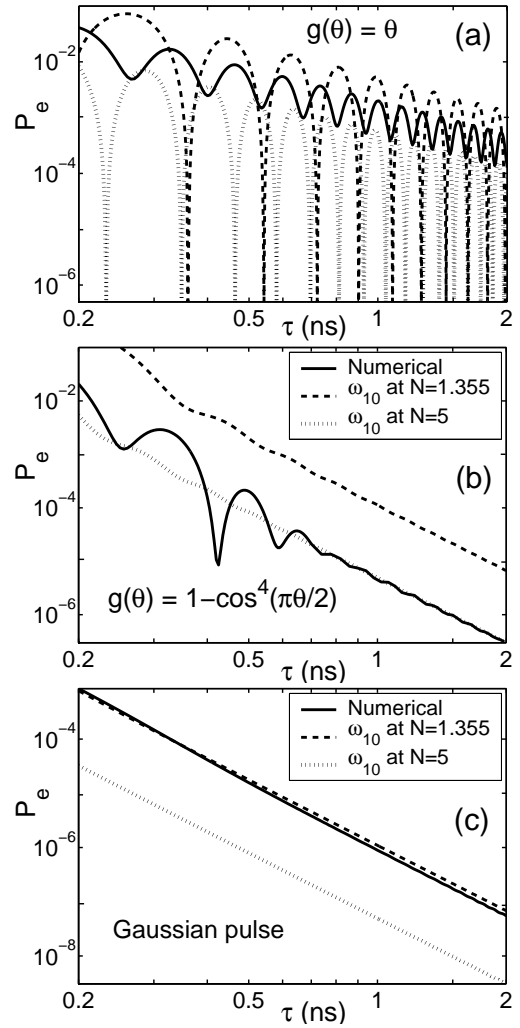

FIG. 5: Dependence of the measurement error P_e on the pulse duration τ calculated either numerically (solid lines) or using the simple formula (28), in which the spectral component is taken at the frequency ω_{10} corresponding to either beginning (dotted lines) or end (dashed lines) of the measurement pulse. The pulse is (a) linear, $g(\theta) = \theta$, (b) of the shape $g(\theta) = 1 - \cos^4(\pi\theta/2)$, or (c) of Gaussian shape. For the Gaussian pulse τ is defined as the r.m.s. width of the pulse.

r_ω^7 is already more than an order of magnitude.] Notice that P_e for the Gaussian pulse [Fig. 5(c)] scales with τ as τ^{-4}, and not in a Gaussian way, as might be naively expected since Fourier transform of a Gaussian is a Gaussian. The reason is that in our case we should use only the rising half of the Gaussian pulse, for which Fourier transform scales with frequency only as ω^{-2}.

The numerically calculated dependence $P_e(\tau)$ for several pulse shapes [shown in Fig. 6(a)] is presented in Fig. 6(b). We consider the following shapes $g(\theta)$:

$$\theta, \ \sin(\pi\theta/2), \ 1 - \cos(\pi\theta/2),$$
$$\sin^2(\pi\theta/2), \ \sin^4(\pi\theta/2), \ 1 - \cos^4(\pi\theta/2). \quad (39)$$

The long-τ behavior of the curves in Fig. 6(b) can be
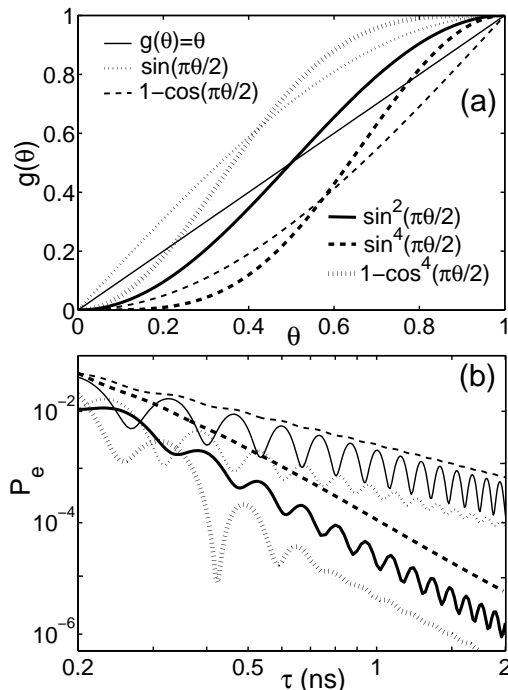
FIG. 6: (a) Several shapes of the measurement pulse and (b) the corresponding dependences $P_e(\tau)$. The pulse shapes are $g(\theta) = \theta$ (thin solid line), $\sin(\pi\theta/2)$ (thin dotted line), $1-\cos(\pi\theta/2)$ (thin dashed line), $\sin^2(\pi\theta/2)$ (thick solid line), $\sin^4(\pi\theta/2)$ (thick dashed line), and $1-\cos^4(\pi\theta/2)$ (thick dotted line).

checked to satisfy Eq. (31). In particular, at long τ the error decays approximately as τ^{-2j} where j [defined right after Eq. (31) as the lowest order of nonvanishing derivatives at the pulse endpoints] is equal to 1 or 2 for the shapes shown in the first or second lines of Eq. (39), respectively (thin and thick lines in Fig. 6). By designing pulses to be even smoother at the endpoints (having larger j) the decay of P_e with increasing τ can formally be made even faster. However, this does not make much practical sense because for long τ the error is very small anyway, and because the derivation of Eq. (31) required an assumption that the pulse shape is described by an analytical function; this assumption can hardly be applied to an experimental situation.

From experimental point of view the most interesting range of P_e is $10^{-4} - 10^{-2}$ (recall that the real measurement error can be up to $Q_e = \sqrt{P_e}$). We see that in this range P_e still significantly depends on the shape of the pulse. Therefore, for a fast and reliable measurement the choice of a proper pulse shape can be really important. Notice that the oscillating behavior of $P_e(\tau)$ dependence for some shapes can in principle be used to minimize nonadiabatic measurement error by choosing specific duration of the measurement pulse.

IV. DISCRIMINATION BETWEEN QUBIT STATES BY TUNNELING

In this section we neglect the nonadiabatic error discussed above and consider the measurement error arising during the tunneling stage of the measurement process. Ideally, the system in state $|1\rangle$ should tunnel from the left to the right well of the qubit potential (Fig. 1), while state $|0\rangle$ should remain in the left well. However, since the ratio of tunneling rates Γ_1/Γ_0 for the two states is finite, discrimination between the states by tunneling is not complete: for a too short measurement pulse there is a chance that the state $|1\rangle$ remains in the left well, while for a too long pulse there is a chance that the state $|0\rangle$ tunnels out.

To take tunneling into account we consider the exact potential (2) and still assume qubit parameters of Eq. (7). Figure 7 shows the dependence of the energy spectrum on the applied flux ϕ. The flux is normalized by the critical value ϕ_c at which the barrier between the two wells disappears (for our parameters $\phi_c = 5.43$). Zero of the energy is chosen at the bottom of the left well for $\phi < \phi_c$ and at the point of inflection of the potential[10] $\delta_c = \pi/2 + \arcsin(1/\lambda)$ for $\phi \geq \phi_c$. The dashed line shows the barrier height, which satisfies quite well the cubic-potential approximation[9,10,11] $\Delta U_l \propto (1-\phi/\phi_c)^{3/2}$. This line separates states above the barrier which are delocalized and states under the barrier which are localized either in the left well or in the right well. In Fig. 7 almost horizontal branches are the left-well states. They are denoted on the left side of the frame as $|k\rangle$ ($k = 0, 1, \dots$), where k enumerates the left-well states. The branches with a steep slope below the barrier top correspond to the right-well states. At $\phi > \phi_c$ the potential represents a single well. Notice the (anti)crossings between energy levels belonging to the left and right wells. In the case when the energy relaxation and dephasing are sufficiently weak so that the corresponding broadening of the right-well levels is smaller than their energy separation, the level crossings correspond to enhanced tunneling from the left well.

For simplicity, let us first neglect the level discreteness in the right well and calculate the tunneling rates Γ_1 and Γ_0 for states $|1\rangle$ and $|0\rangle$ using WKB approximation. Then $\Gamma_k = f_a(k)D(k)$, where WKB factor $D(k) = \exp[-(2/\hbar) \int_{\delta_{t1}}^{\delta_{t2}} \sqrt{2m(U(\delta) - \tilde{E}_k)} \, d\delta]$ is determined by the integral between classical turning points δ_{t1} and δ_{t2} (we use notation $\tilde{E}_k$ for the energy of the qubit state $|k\rangle$ to distinguish it from notation E_k used in Sections II and III). For the attempt frequency $f_a(k)$ we use approximation[20] $f_a(k) = (\omega_l/2\pi)[(2\pi)^{1/2}/k!][(k+1/2)/e]^{k+1/2}$, where ω_l is the left-well plasma frequency. (Even though this formula has been derived[20] for the case when there are many levels in the well, and so it is not quite accurate in our case, the inaccuracy is not very significant for us.) Figure 8 shows the tunneling rates Γ_1 and Γ_0 as functions of ϕ/ϕ_c. The lines end when the cor-
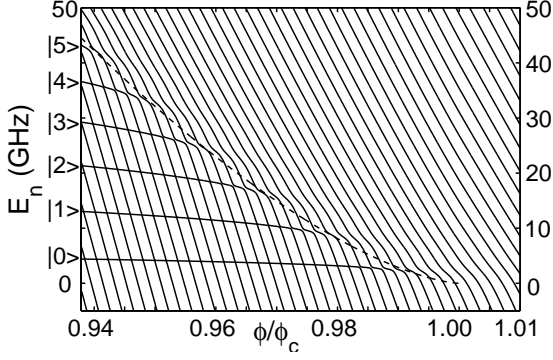
FIG. 7: Structure of the energy levels E_n (in GHz) as a function of external flux ϕ (in units of critical flux $\phi_c = 5.43$). The levels with n between 168 and 218 (counted from the right-well bottom) are shown. The dashed line shows the barrier height ΔU_l. The vectors $|k\rangle$ on the left enumerate the states localized in the left well.
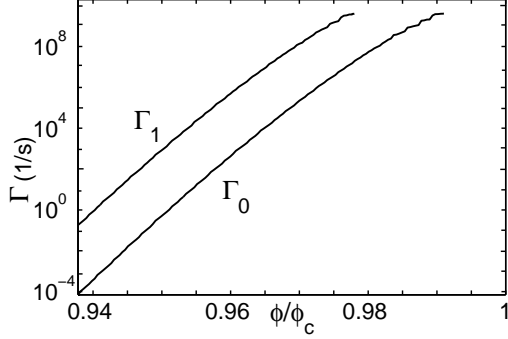

FIG. 8: The WKB tunneling rates Γ_1 and Γ_0 for the states $|1\rangle$ and $|0\rangle$ as functions of the applied flux ϕ.
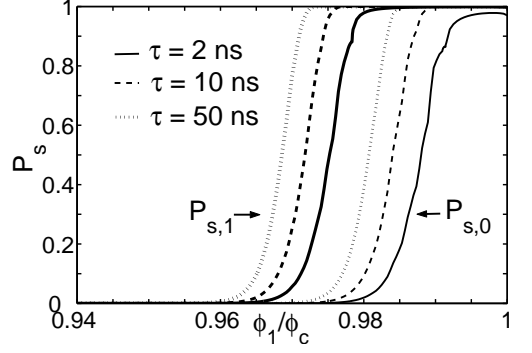

FIG. 9: The probabilities $P_{s,1}$ (thick lines) and $P_{s,0}$ (thin lines) of tunneling to the right well during the measurement pulse, starting from the states $|1\rangle$ or $|0\rangle$, correspondingly, as functions of the maximum flux ϕ_1 during the pulse. Calculations are based on the WKB approximation. Initial flux is $\phi_0/\phi_c = 0.94$ ($N = 5$). The pulse duration is $\tau = 2$ ns (solid lines), 10 ns (dashed lines), or 50 ns (dotted lines).

responding levels reach the barrier top. Small steps near the ends of the lines are due to level anticrossings. One can see that the ratio Γ_1/Γ_0 decreases with increasing flux ϕ and is slightly over 10^2 in the practically interesting range where $\Gamma_1 \gtrsim 10^8$ s^{-1}.

Since the applied flux ϕ changes during the measurement pulse, the tunneling should be integrated over the pulse duration. For definiteness let us consider the parabolic measurement pulse

$$\phi(t) = \phi_0 + 4(\phi_1 - \phi_0)(t/\tau)(1 - t/\tau) \ \ (0 \leq t \leq \tau), \ (40)$$

so that the flux $\phi(t)$ increases from ϕ_0 to the maximal value ϕ_1 at $t = \tau/2$ and then decreases back to ϕ_0 at $t = \tau$. (Notice a different definition of the pulse duration τ compared to the definition used in Sec. III, in which we considered only half-pulses.) Figure 9 shows the probabilities of tunneling during the measurement pulse (switching to the right well) $P_{s,1}$ and $P_{s,0}$ for levels $|1\rangle$ and $|0\rangle$,

$$P_{s,k} = 1 - \exp\left[-\int_0^\tau \Gamma_k(t)\,dt\right], \qquad (41)$$

as functions of the maximum flux ϕ_1 (normalized by critical flux $\phi_c = 5.43$); initial flux $\phi_0 = 5.09$ ($\phi_0/\phi_c = 0.94$) corresponds to $N = 5$; the pulse durations are $\tau = 2$ ns, 10 ns, and 50 ns. Notice that Γ_k is not well-defined when the state goes over the barrier, while we need some value of Γ_k for integration in Eq. (41); in this case we still use the definition $\Gamma_k = f_a(k)D(k)$ but assume $D(k) = 1$. The curves in Fig. 9 remain at practically zero level for small pulse amplitudes and saturate at 100% level for large enough pulse amplitude (the "S-curve" shape). (The switching probability $P_{s,0}$ for $\tau = 2$ ns does not fully approach 100% because the pulse duration is too short.) The most important observation is that the flux shift between the curves for $P_{s,1}$ and $P_{s,0}$ (for the same τ) is sufficiently large to reliably distinguish states $|1\rangle$ and $|0\rangle$. However, the measurement error, which can be defined as $(P_{s,0} + 1 - P_{s,1})/2$, is finite for any ϕ_1, and in the optimal point is on the order of 10^{-2}. (Actually, our method is not quite accurate for the top part of the S-curves because of significant level anticrossings, which leads to visible kinks on the curves in Fig. 9 and inaccuracy of the measurement error calculation.) One can see that the minimal measurement error improves (decreases) with increase of the pulse duration τ; even though the separation of the two S-curves decreases with increase of τ, they become sharper, leading to better discrimination between states $|1\rangle$ and $|0\rangle$.

The WKB approximation does not take into account the level discreteness in the right well. To take it into account, we have performed the full quantum-mechanical simulation of the evolution (4)–(5) during the measurement pulse (40). Since the level broadening is determined by energy relaxation (and dephasing), which is very difficult to simulate exactly, we have used a simpler model. We assume that the levels in the right well and above the barrier have a finite lifetime (complex energy), while levels in the left well do not decay. The decay rate for

the nth level counting from the bottom of the right well is chosen as $\gamma = n/T_1$, where T_1 is the energy relaxation time; the corresponding width of the broadened level is $\hbar\gamma$. Since there are many levels in the right well and we are interested only in levels close to the barrier top, the level index n can be replaced with the number of levels N_r in the right well; for the parameters (7) which we use, $N_r = 174$ at $N = 5$. [Actually, there are some additional details in the algorithm. For example, to prevent unphysical decay of the left-well state during the level crossing, we smoothly (parabolically) suppress γ when the energy distance to the nearest level becomes less than $1/5$ of the normal level separation in the right well. The numerical criterion for a left-well level is that its energy is in between the left well bottom and the barrier top, and also the maximum of the wavefunction is to the left of the barrier top.]

Solid lines in Fig. 10 show the numerically calculated probability $P_{s,k}$ of switching to the right well during the measurement pulse (starting with $N = 5$, $\phi/\phi_c = 0.94$) in the case when initially either the left-well ground state ($k = 0$) or the first excited state ($k = 1$) is occupied. Assumed pulse duration is $\tau = 2$ ns, while $T_1 = 60$ ns. Switching probability is defined as $P_s = 1 - P_l$, where P_l is the total population of the left-well levels after the pulse. One can see that the numerical dependence $P_{s,k}(\phi)$ is generally similar to the corresponding WKB result (dashed lines); however, the numerical curves show significant oscillations due to level discreteness in the right well. Notice that the amplitude of oscillations in this case is mainly determined not by the width of the levels (which is still relatively small in this example), but by continuous sweeping through the comb of levels during the pulse. (For our parameters the level broadening becomes larger than the level spacing at $T_1 \lesssim 5$ ns.) Similar oscillations in the dependence $P_{s,k}(\phi_1)$ have been observed experimentally,[21] though for a qubit with a smaller number of levels in the right well ($N_r \sim 30$, in contrast to $N_r \sim 170$ in the example shown in Fig. 10), that leads to a smaller level broadening $\hbar\gamma \simeq \hbar N_r/T_1$ and therefore more pronounced effects of the right-well level discreteness.

Figures 8–10 show that the quality of tunneling discrimination between states $|1\rangle$ and $|0\rangle$ depends significantly on the choice of the measurement pulse amplitude (maximum flux ϕ_1), and at the optimal point the measurement error $(P_{s,0} + 1 - P_{s,1})/2$ is on the order of 10^{-2}. This error decreases for longer measurement pulses and can be further reduced by changing the qubit parameters.

V. LEFT WELL REPOPULATION

A steady progress in fabrication of phase qubits has resulted in a significant decrease of the dissipation rate.[22] This trend will obviously continue because of the requirement of very low decoherence in quantum computation. Therefore it is of interest to study the measurement pro-
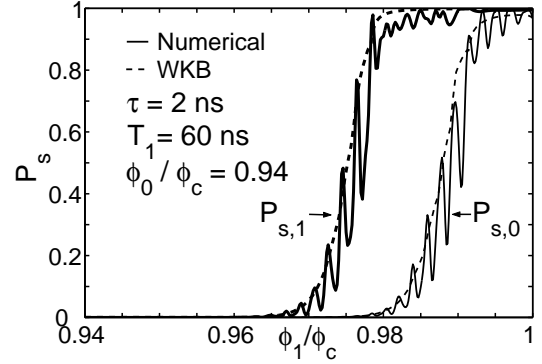

FIG. 10: The switching probabilities $P_{s,0}$ (thin lines) and $P_{s,1}$ (thick lines) as functions of the maximum flux ϕ_1, calculated numerically (solid lines) and using WKB approximation (dashed lines). The measurement pulse is of parabolic shape with duration $\tau = 2$ ns, starting and ending at flux $\phi_0/\phi_c = 0.94$ ($N = 5$). Oscillations of the solid lines reflect level discreteness in the right well. (At $N = 5$ there are $N_r = 174$ levels in the right well.)

cess for a phase qubit with a very long energy relaxation time T_1. Let us we consider the limit of negligible dissipation, $T_1 = \infty$. As we will see below, in this case the results are qualitatively different from the results discussed in the previous section. The most important effect is that the switching probability $P_{s,k}$ does not approach 100% even for measurement pulses with maximum flux ϕ_1 well above the critical value ϕ_c, in contrast to what is shown in Figs. 9 and 10.

To demonstrate this effect, let us assume that initially the system is in the left-well ground state $|0\rangle$ and simulate the full quantum evolution (4)–(5) during the measurement pulse (40). Figure 11 (the main frame) shows the populations $P_n(t)$ of levels n (levels are counted from the right-well ground state) with $169 \leq n \leq 204$ for the measurement pulse with initial flux $\phi_0 = 0.94\phi_c$ (corresponding to $N = 5$), maximum flux $\phi_1 = 1.01\phi_c$, and total duration $\tau = 2$ ns. The inset shows the structure of energy levels E_n (for $168 \leq n \leq 218$) as a function of time during the first (increasing) half of the pulse (the only difference between Fig. 7 and the inset of Fig. 11 is the converted horizontal axis). The state $|0\rangle$ initially corresponds to $n = 169$.

The population of the qubit state $|0\rangle$ can be seen as the upper envelope dependence of $P_n(t)$ for $t < 0.63$ ns; similarly, lower envelope curve at $t < 0.4$ ns corresponds to the state $|1\rangle$. At $t < 0.4$ ns the state $|0\rangle$ is sufficiently deep in the left well, so that the level splittings in the avoided crossings are too small to cause transitions from this level to the right well (notice though the change of the level number corresponding to $|0\rangle$ after each level crossing). As a result, at $t < 0.4$ ns the populations of levels $|0\rangle$ and $|1\rangle$ vary only due to the nonadiabatic effects (see Sec. III).

At $0.4 < t < 0.63$ ns there is an appreciable probability of a transition to the right well at each crossing of the
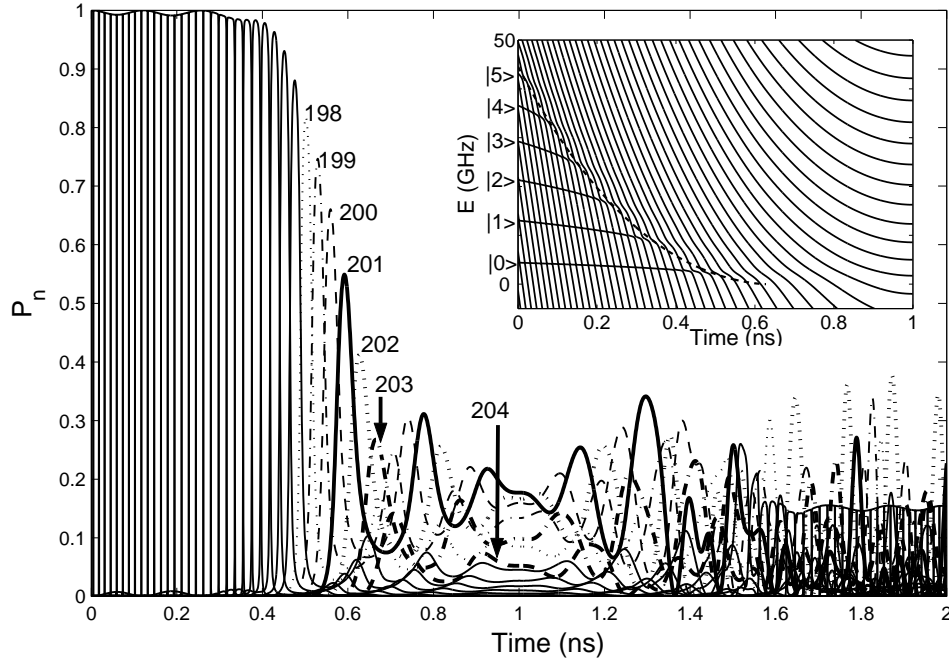
FIG. 11: The level populations P_n ($169 \leq n \leq 204$) as functions of time t for the measurement pulse with duration $\tau = 2$ ns, starting and ending at $\phi_0/\phi_c = 0.94$ ($N = 5$) with maximum flux in the middle $\phi_1/\phi_c = 1.01$. The curves for $169 \leq n \leq 197$ are thin solid lines, the curves for $198 \leq n \leq 204$ are denoted by the value of n. Inset: Energies E_n ($168 \leq n \leq 218$) versus time t for the rising part of the pulse (similar to Fig. 7).

qubit level $|0\rangle$ with a right-well level. In this time interval one can still interpret the envelope of the populations of the crossing states as the population of state $|0\rangle$, despite the level $|0\rangle$ becomes above the barrier at $t > 0.5$ ns (see the inset). We have checked numerically that the transition probabilities at the level crossings agree with the Landau-Zener formula[18]. At $t < 0.5$ ns, when the state $|0\rangle$ is still below the barrier, the transitions to the right well are due to tunneling. At $t > 0.5$ ns the level splittings increase and become comparable to the separations between adjacent right-well levels; this means that generally more than two levels are coupled simultaneously. At $t > 0.63$ ns the left well disappears (see the inset), and the initial population of level $|0\rangle$ becomes distributed between several states in the resulting single well.

During the time interval when the potential (2) has a single-well shape (0.63 ns $< t <$ 1.37 ns), one can see a rather significant and complicated redistribution of the level population. Notice that the most populated levels in the single well are those with $198 \leq n \leq 204$, i.e., with the quantum number significantly higher than the initial $n = 169$. The solid line in Fig. 12 shows the population distribution at $t = 1$ ns (middle of the pulse); one can see that the population is noticeable only for $n \geq 192$, which are the states delocalized (above-the-barrier) before and after the pulse.

After $t = 1$ ns the pulse starts to decrease, and the potential (2) starts to return to its initial shape. The levels localized in the left well start to appear again and
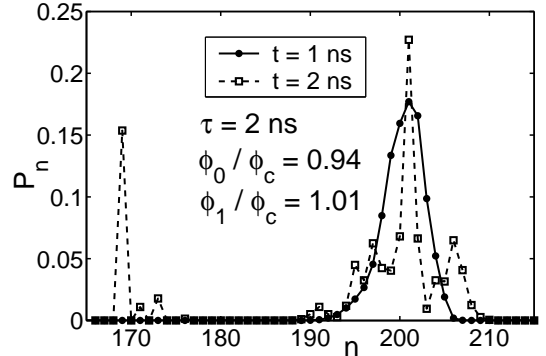

FIG. 12: The level populations P_n at $t = 1$ ns and $t = 2$ ns for the process shown in Fig. 11 ($\phi_1/\phi_c = 1.01$, $\tau = 2$ ns). The data are shown by dots and squares, connected by lines as guides for the eye.

cross with the populated right-well levels which are moving up. As a result, the qubit state $|0\rangle$ partially recovers its population (in Fig. 11 it is seen as an approximately horizontal line after 1.6 ns), and also a number of higher levels in the left well become populated. As the dashed line in Fig. 12 shows, after the end of the pulse an appreciable population is acquired by states $|0\rangle$, $|1\rangle$, and $|2\rangle$ of the left well and also by a number of delocalized states with $n \geq 190$.

In short, during the first half of the pulse, right-well and delocalized levels go down in energy and cross with

left-well levels, thus gaining population, while during the second half of the pulse, right-well levels move up and cross again with left-well levels, resulting in a partial repopulation of the initial state and an excitation of higher levels. Naively, one could expect that after such strong measurement pulse the population should be transferred from the left well to the right well. However, we see that without dissipation the population actually goes mainly to highly excited delocalized states. Assuming a very small but finite dissipation after the pulse, we conclude that a populated delocalized state will eventually end up either in the left or in the right well. Therefore, there are two contributions to the left well repopulation: direct repopulation (due to level crossings) and relaxation from delocalized states.

After the pulse the probability for the system to be to the right of the barrier top is

$$P_r(t) = \int_{\delta_m}^{\infty} |\Psi(\delta, t)|^2 d\delta \qquad (42)$$

(where δ_m is the barrier-top position), and generally depends on time due to interference of occupied delocalized levels. We define the probability of escape (switching) to the right well as the time average of $P_r(t)$. Thus, the switching probability is given by

$$P_s = \sum_n P_n \int_{\delta_m}^{\infty} |\psi_n(\delta)|^2 d\delta, \qquad (43)$$

where P_n is the population of level n after the pulse, and the integral is the probability for the system in state n to be in the right well. This integral equals zero (one) for states localized in the left (right) well and is between 0 and 1 for delocalized states.

The solid line in Fig. 13(a) shows the dependence of the switching probability $P_{s,0}$ (starting from state $|0\rangle$) on the maximum flux ϕ_1 for $\tau = 2$ ns and $\phi_0/\phi_c = 0.94$. The switching probability practically vanishes at $\phi_1/\phi_c < 0.98$ when the initial state $|0\rangle$ remains sufficiently deep inside the left well and cannot tunnel (similar to the results shown in Figs. 9 and 10). However, in contrast to Figs. 9 and 10, an increase of the pulse amplitude leads to significant and irregular oscillations of $P_{s,1}(\phi_1)$. Most importantly, the switching probability remains to be significantly less than 100% even for ϕ_1 exceeding ϕ_c.

The solid line in Fig. 13(b) shows the switching probability $P_{s,0}$ as a function of the pulse duration τ for $\phi_1 = \phi_c$. The dependence is even more irregular than in Fig. 13(a). The irregular oscillations seen in Figs. 13(a) and 13(b) can be related to the complicated time dependence of the level populations seen in Fig. 11.

Besides calculations for the qubit parameters shown in Eq. (7), we have also considered a different set of qubit parameters:

$$C = 790 \text{ fF}, \ L = 0.720 \text{ nH}, \ I_0 = 0.764 \ \mu\text{A}. \qquad (44)$$

The main difference between the two sets is a significantly different number of levels in the right well. For the initial
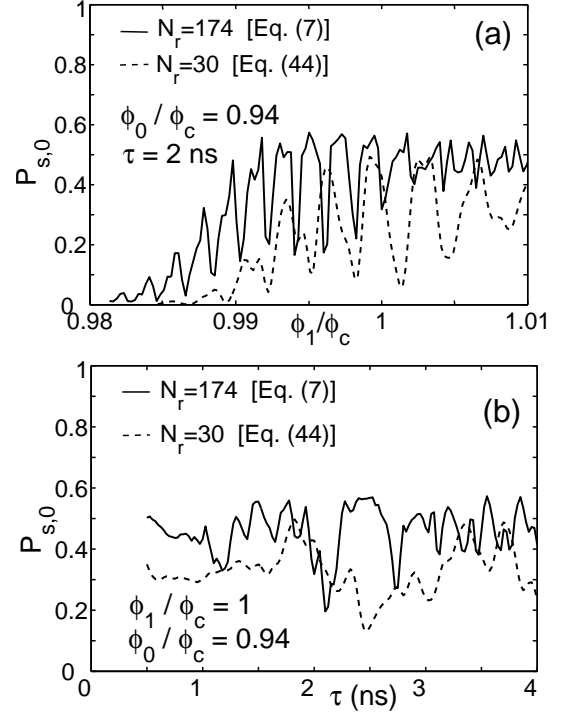

FIG. 13: The switching probability $P_{s,0}$ for the initial state $|0\rangle$ [see Eq. (43)] (a) versus the maximum flux ϕ_1 (normalized by the critical flux ϕ_c) for $\tau = 2$ ns and (b) versus the pulse duration τ for $\phi_1 = \phi_c$. Solid lines are for our usual set (7) of qubit parameters; dashed lines are for the qubit with parameters (44), having much smaller number N_r of discrete levels in the right well.

condition $N = 5$, the number of levels N_r in the right well is $N_r = 174$ for our main set of parameters (7) and $N_r = 30$ for the parameters (44). The eigenenergies of the Hamiltonian as functions of flux ϕ for the parameter set (44) are shown in Fig. 14 (flux is normalized by the critical flux $\phi_c = 3.55$).

In spite of a significant difference of the energy level structure, the behavior of the switching probability $P_{s,0}$ shown in Figs. 13(a) and 13(b) by dashed lines for the parameter set (44) is qualitatively similar to the previously discussed behavior for the set (7) (solid lines). Notice, however, that in a real experiment the effective time $\gamma^{-1} \simeq T_1/N_r$ spent on a right-well level before relaxation is significantly larger for the set (44) and therefore the discussed here effects due to insufficiently fast relaxation will be more pronounced.

It is important to notice that while the large irregular oscillations of switching probability P_s in Fig. 13 is a result of quantum interference and therefore will be significantly suppressed by a weak relaxation, the fact that P_s does not approach 100% even for $\phi_1 > \phi_c$ [as for curves in Fig. 13(a)] is a much more robust, essentially classical effect. Our results show that a very significant repopulation of the left well may occur if the dissipation is insufficiently fast. In other words, sufficiently strong
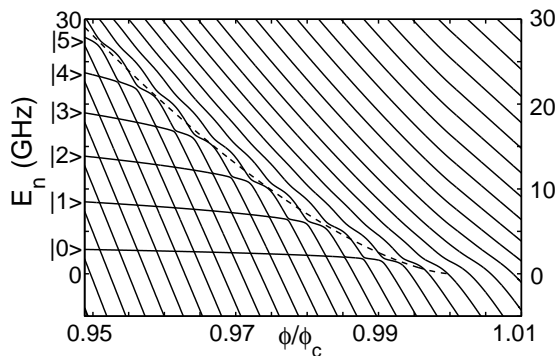
FIG. 14: Energies E_n (in GHz) as a function of flux ϕ (in units of $\phi_c = 3.55$) for the qubit with parameters (44) corresponding to $N_r = 30$. The levels with $24 \leq n \leq 57$ are shown. The dashed line corresponds to the barrier height ΔU_l.

energy dissipation is a necessary requirement for a good measurement fidelity. Conversely, the repopulation effect imposes a lower limit on the pulse duration for a given dissipation rate.

Let us estimate the condition necessary to eliminate the left-well repopulation. For simplicity, we assume the pulse to be almost rectangular, with the rise and fall times being significantly shorter than the time τ_m, during which the pulse is at its maximum. Let us denote by n_i the level number (counting from the right-well ground state), corresponding to the right-well level close to the top of the barrier for maximum flux bias. Assume that this level is populated immediately after the pulse rise. Then during τ_m the energy relaxation will lead to the decrease of n-number corresponding to the mostly populated level. Neglecting the "energy diffusion" of the populated levels, we estimate the n-number at time τ_m as $n_i' \simeq n_i - \gamma\tau_m$, where γ is the transition rate between adjacent levels. We neglect the weak dependence of γ on the level number. Let n_f be the first level above the barrier top after the pulse is over. If we neglect a change of n_i' during the falling part of the pulse, the condition that there is no return to the left well is $n_i' < n_f$, which means $\tau_m > (n_i - n_f)/\gamma$. Using an estimate $\gamma \simeq n_i/T_1$, we obtain

$$\tau_m > \frac{n_i - n_f}{n_i}\, T_1. \qquad (45)$$

This condition is actually a lower bound; the required pulse duration τ_m can be even longer because of not immediate population of the level n_i, widening of the range of populated levels in the course of relaxation ("energy diffusion"), and possibility of repopulation due to tunneling. For the case shown in Figs. 11 and 12 we find $n_i = 205$, $n_f = 181$, yielding $\tau_m > 0.13\, T_1$.

The necessity of sufficiently long measurement pulses thus seems to be an important requirement for the design of quantum gates based on phase qubits. It also makes harder the solution of the cross-talk problem[6,10] for simultaneous measurement of several qubits, which argues in favor of designing adjustable coupling between qubits.

VI. CONCLUSION

In this paper we have studied the behavior of a flux-biased phase qubit in the process of its measurement (using analytical approaches and numerical solution of the Schrödinger equation) and analyzed several mechanisms leading to measurement errors.

First, we have studied nonadiabatic errors (Sec. III), which occur during the rising part of the measurement pulse (before the tunneling stage) due to finite duration of the pulse, leading to the transitions between qubit states $|1\rangle$ and $|0\rangle$. We have developed simplified analytical approaches with several levels of accuracy [see Eqs. (25), (27), and (28)] and compared them with the numerical results (Sec. III B). The nonadiabatic error generally decreases with increase of the pulse duration τ; however, this dependence may exhibit significant oscillations. The numerical value of the error depends significantly on the pulse shape (Figs. 5 and 6), thus showing importance of a proper pulse shape design. For pulse duration over few nanoseconds the nonadiabatic error is typically sufficiently small to be considered negligible.

Another type of measurement error is due to incomplete discrimination between states $|1\rangle$ and $|0\rangle$ during the tunneling stage of the measurement process (Sec. IV). For typical qubit parameters[6] the ratio of WKB tunneling rates Γ_1/Γ_0 for states $|1\rangle$ and $|0\rangle$ is few times 10^2 and decreases with the applied flux bias (i.e. when faster measurement is required). Therefore, the minimized (over the maximum applied flux during measurement) measurement error is smaller for longer pulses (Fig. 9). The level discreteness in the right well of the qubit potential [Fig. 1(b)] leads to oscillations in the dependence of the switching probability on the measurement pulse amplitude (Fig. 10). A typical value of the minimized error due to incomplete discrimination between the states by tunneling is on the order of 10^{-2} for typical qubit parameters of present-day experiments.[6] Change of qubit design may lead to further reduction of this type of measurement error.

In Sec. V we have analyzed the quantum evolution of the qubit during its measurement in the case of complete absence of energy relaxation, and found that the energy relaxation plays a very important role in the process of qubit measurement. In the case of insufficiently fast dissipation (characterized by energy relaxation time T_1) the measurement error can be caused by the repopulation of the left well of the qubit potential [Fig. 1(b)] after the tunneling stage of the measurement process. A simple estimate (45) for the repopulation effect shows that reliable measurement requires relatively long measurement pulses; in the analyzed example the pulse should be longer than $\sim 0.1\, T_1$. This result may be quite important for the design of the quantum gates based on phase qubits. Some alleviation of the problem may be achieved

by using a different shape of the measurement pulse, so that the barrier height of the qubit potential after the pulse is significantly lower than before the measurement.

[*] Permanent address: Department of Chemical Physics, The Weizmann Institute of Science, Rehovot 76100, Israel

[1] Y. Nakamura, Yu. A. Pashkin, and J. S. Tsai, Nature **398**, 786 (1999); D. Vion D, A. Aassime, A. Cottet, P. Joyez, H. Pothier, C. Urbina, D. Esteve,and M. H. Devoret, Science **296**, 886 (2002); T. Duty, D. Gunnarsson, K. Bladh, and P. Delsing, Phys. Rev. B **69**, 140503(2004); A. Guillaume, J. F. Schneiderman, P. Delsing, H. M. Bozler, and P. M. Echternach, Phys. Rev. B **69**, 132504 (2004); A. Wallraff, D. I. Schuster, A. Blais, L. Frunzio, J. Majer, M. H. Devoret, S. M. Girvin, and R. J. Schoelkopf, Phys. Rev. Lett. **95**, 060501 (2005).

[2] I. Chiorescu, Y. Nakamura, C. J. P. M. Harmans, and J. E. Mooij, Science **299**, 1869 (2003); J. R. Friedman, V. Patel, W. Chen, S. K. Tolpygo, and J. E. Lukens, Nature **406**, 43 (2000).

[3] J. M. Martinis, S. Nam, J. Aumentado, and C. Urbina, Phys. Rev. Lett. **89**, 117901 (2002); Y. Yu, S. Han, X. Chu, S.-I Chu, and Z. Wang, Science **296**, 1869 (2002); A. J. Berkley, H. Xu, M. A. Gubrud, R. C. Ramos, J. R. Anderson, C. J. Lobb, and F. C. Wellstood, Phys. Rev. B **68**, 060502(R) (2003).

[4] Yu. A. Pashkin, T. Yamamoto, O. Astafiev, Y. Nakamura, D. V. Averin, and J. S. Tsai, Nature **421**, 823 (2003); T. Yamamoto, Yu. A. Pashkin, O. Astafiev, Y. Nakamura, and J. S. Tsai, Nature **425**, 941 (2003).

[5] A. J. Berkley, H. Xu, R. C. Ramos, M. A. Gubrud, F. W. Strauch, P. R. Johnson, J. R. Anderson, A. J. Dragt, C. J. Lobb, and F. C. Wellstood, Science **300**, 1548 (2003).

[6] R. McDermott, R. W. Simmonds, M. Steffen, K. B. Cooper, K. Cicak, K. D. Osborn, S. Oh, D. P. Pappas, and J. M. Martinis, Science **307**, 1299 (2005).

[7] K. B. Cooper, M. Steffen, R. McDermott, R. W. Simmonds, S. Oh, D. A. Hite, D. P. Pappas, and J. M. Martinis, Phys. Rev. Lett. **93**, 180401 (2004).

[8] R. W. Simmonds, K. M. Lang, D. A. Hite, S. Nam, D. P. Pappas, and J. M. Martinis, Phys. Rev. Lett. **93**, 077003 (2004); N. Katz, M. Ansmann, R. C. Bialczak, E. Lucero, R. McDermott, M. Neeley, M. Steffen, E. M. Weig, A. N. Cleland, J. M. Martinis, and A. N. Korotkov, Science **312**, 1498 (2006).

[9] P. R. Johnson, W. T. Parsons, F. W. Strauch, J. R. Anderson, A. J. Dragt, C. J. Lobb, and F. C. Wellstood, Phys. Rev. Lett. **94**, 187004 (2005); *ibid.* **95**, 049901(E) (2005).

[10] A. G. Kofman, Q. Zhang, J. M. Martinis, and A. N. Korotkov, cond-mat/0606078.

[11] K. K. Likharev, *Dynamics of Josephson Junctions and Circuits* (Gordon and Breach, New York, 1986); T. Van Duzer and C. W. Turner, *Principles of Superconductive Devices and Circuits* (Elsevier, New York, 1981).

[12] C. Y. Chen, J. Phys. A **35**, 6589 (2002).

[13] C. C. Marston and G. G. Balint-Kurti, J. Chem. Phys. **91**, 3571 (1989).

[14] B. Fornberg, *A Practical Guide to Pseudospectral Methods* (Cambridge University Press, Cambridge, 1996).

[15] We use the same value $N = 1.355$ as in our previous paper[10] for the two-qubit setup. Since in the present paper the effective junction capacitance is a little smaller (because we do not have coupling capacitance $C_x = 6$ fF), the state $|1\rangle$ for $N = 1.355$ is actually slightly above the barrier for the potential (2). However, for the modified potential (8) used in Section III the state $|1\rangle$ is still below the barrier for $N = 1.355$.

[16] B. R. Holstein, *Topics in Advanced Quantum Mechanics* (Addison-Wesley, Redwood City, 1992).

[17] K. Gottfried and T.-M. Yan, *Quantum Mechanics: Fundamentals* (Springer, New York, 2003).

[18] L. D. Landau and E. M. Lifshitz, *Quantum Mechanics: Non-Relativistic Theory* (Pergamon Press, Oxford, 1977).

[19] L. M. Garrido and F. J. Sancho, Physica **28**, 553 (1962); F. J. Sancho, Proc. Phys. Soc. **89**, 1 (1966).

[20] K. K. Likharev, Physica **108B**, 1979 (1981).

[21] N. Katz *et al.*, to be published.

[22] J. M. Martinis, K. B. Cooper, R. McDermott, M. Steffen, M. Ansmann, K. D. Osborn, K. Cicak, S. Oh, D. P. Pappas, R. W. Simmonds, and C. C. Yu, Phys. Rev. Lett. **95**, 210503 (2005).